
This is the **accepted manuscript** of the following article:

Perez-Calleja, P., Aybar, M., Piciooreanu, C., Esteban-Garcia, A. L., Martin, K. J., & Nerenberg, R. (2017). Periodic venting of MABR lumen allows high removal rates and high gas-transfer efficiencies. *Water Research*, 121:349-360.

The manuscript has been published in final form at:

<https://doi.org/10.1016/j.watres.2017.05.042>

1 **Periodic venting of MABR lumen allows high removal rates**
2 **and high gas-transfer efficiencies**

3

4 P. Perez-Calleja ^{a,b}, M. Aybar ^{a,c}, C. Picioreanu ^d, A.L. Esteban-Garcia ^b, K.J. Martin ^e,
5 R. Nerenberg ^{a*}

6 ^a University of Notre Dame, Department of Civil and Environmental Engineering and Earth
7 Sciences 156 Fitzpatrick Hall, Notre Dame, IN 46556, USA. nerenberg.1@nd.edu,
8 maybar@nd.edu, pperezca@nd.edu

9 ^b University of Cantabria, Department of Sciences and Techniques of Water and the
10 Environment, University of Cantabria, Avda. Los Castros s/n, 39005 Santander, Spain.
11 analorena.esteban@unican.es, pperezca@nd.edu

12 ^c Department of Civil Engineering, University of Concepcion, Casilla 160-C, Ciudad
13 Universitaria, Concepcion, Chile. maybar@udec.cl

14 ^d Department of Biotechnology, Faculty of Applied Sciences, Delft University of Technology,
15 Van der Maasweg 9, 2629 HZ, Delft, The Netherlands. c.picioreanu@tudelf.nl

16 ^e Black and Veatch, 8400 Ward Parkway, Kansas City, Missouri 64114, USA.
17 MartinKJ@bv.com

18

19 *Corresponding author

20 E-mail address: nerenberg.1@nd.edu (R. Nerenberg)

21

22

23

24

25

26 **ABBREVIATIONS**

27 DO – Dissolved oxygen

28 GTE – Gas transfer efficiency

29 GTR – Gas transfer rate

30 J – Contaminant removal flux

31 HFM – Hollow-fiber membrane

32 MABR – Membrane-aerated biofilm reactor

33 MBfR – Membrane-biofilm reactor

34 **ABSTRACT**

35 The membrane-aerated biofilm reactor (MABR) is a novel treatment technology that
36 employs gas-supplying membranes to deliver oxygen directly to a biofilm growing on
37 the membrane surface. When operated with closed-end membranes, the MABR
38 provides 100-percent oxygen transfer efficiencies (OTE), resulting in significant energy
39 savings. However, closed-end MABRs are more sensitive to back-diffusion of inert
40 gases, such as nitrogen. Back-diffusion reduces the average oxygen transfer rates
41 (OTR), consequently decreasing the average contaminant removal fluxes (J). We
42 hypothesized that venting the membrane lumen periodically would increase the OTR
43 and J. Using an experimental flow cell and mathematical modeling, we showed that
44 back-diffusion gas profiles developed over relatively long timescales. Thus, very short
45 ventings could re-establish uniform gas profiles for relatively long time periods. Using
46 modeling, we systematically explored the effect of the venting interval (time between
47 ventings). At moderate venting intervals, opening the membrane for 20 seconds every
48 30 minutes, the venting significantly increased the average OTR and J without
49 substantially impacting the OTEs. When the interval was short enough, in this case
50 shorter than 20 minutes, the OTR was actually higher than for continuous open-end
51 operation. Our results show that periodic venting is a promising strategy to combine the
52 advantages of open-end and closed end operation, maximizing both the OTR and OTE.

53

54 **KEYWORDS**

55 Hollow-fiber membranes; MBfR; MABR; gas back-diffusion; gas transfer efficiency;
56 gas transfer rate

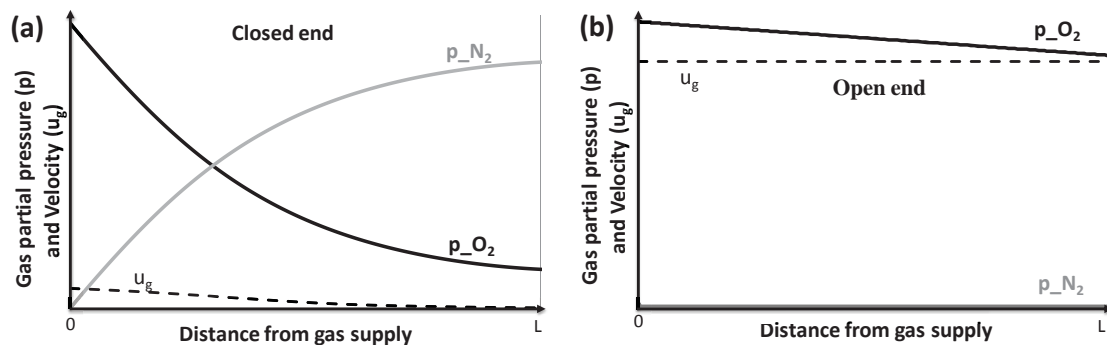
58 **1. INTRODUCTION**

59 Gas-transferring, hollow-fiber membranes (HFM) are commonly used to supply gases
60 for environmental, industrial and medical applications. For example, bundles of HFMs
61 have been used for oxygenation of rivers and water streams, for blood oxygenation, and
62 for bioremediation of groundwater contaminants (Weiss et al., 1998; Roggy et al., 2002;
63 Federspiel and Henchir, 2004). However, an emerging application is the membrane-
64 biofilm reactor (MBfR), where HFMs supply gaseous substrates to a biofilm growing
65 directly on the membrane's outer surface (Martin and Nerenberg, 2012; Nerenberg,
66 2016). When used to deliver air or oxygen, the process is often referred to as the
67 membrane-aerated biofilm reactor (MABR). MABRs can simultaneously remove
68 biological oxygen demand (BOD), nitrify, and denitrify (Timberlake et al., 1988; Hibiya
69 et al., 2003; Terada et al., 2003; Jácome et al., 2006; Matsumoto et al., 2007; Syron and
70 Casey, 2008). Several commercial applications are in development, but very few full-
71 scale applications exist.

72 MABRs can be operated with closed or open-ended HFMs. With closed-ended HFMs,
73 all the oxygen supplied to the membranes is delivered to the biofilm, allowing 100%
74 oxygen transfer efficiencies (OTEs) (Brindle et al., 1998; Pankhania et al., 1999; Hibiya
75 et al., 2003; Terada et al., 2003; Syron and Casey, 2008; Martin and Nerenberg, 2012).
76 This can save up to 85% in energy costs, compared to conventional activated sludge
77 process (Aybar et al., 2014). However, closed-ended HFMs typically suffer from gas
78 back-diffusion, where N_2 and other dissolved gases diffuse into the membrane lumen
79 (Schaffer et al., 1960; Ahmed and Semmens, 1992a). With back-diffusion, the distal
80 end of the membrane may be "deadened," leading to lower average oxygen transfer

81 rates (OTR) compared to open-end operation (Figure 1a). In this paper, we consider
82 OTR to be synonymous with the oxygen flux, J_{O_2} , across the membrane.

83 With open-ended HFMs, the intra-membrane gas velocity is high throughout the
84 membrane. With high velocities, advective mass transport in the lumen is much greater
85 than the diffusive transfer across the membrane wall. This results in more uniform
86 oxygen concentrations in the lumen, leading to high average OTRs (Figure 1b).
87 However, a large amount of gas is lost from open end. Also, the high gas velocity leads
88 to greater frictional pressure losses occurrence along the membrane, resulting in greater
89 energy requirements and lower gas pressures at the distal end of the membrane. For the
90 MABR, lower overall OTR translates into lower average substrate removal fluxes (J).



91

92 **Figure 1.** Schematic showing differences between hollow-fiber membranes at steady-state in: (a) closed-
93 end operation, and (b) open-end operation. In this example, the membrane is pressurized with pure O_2
94 transferring to liquid containing dissolved N_2 . Figures show typical oxygen and nitrogen partial pressures
95 (p_{O_2} and p_{N_2}) and gas velocities (u_g) along the membrane length. The open end membrane has higher p_{O_2}
96 across the entire membrane, leading to higher gas transfer rates, but has low gas transfer efficiencies, as
97 most of the gas is vented through the end.

98

99 Many researchers have explored ways to improve the OTR of HFMs (Weissman and
100 Mockros, 1969; Tanishita et al., 1978; Côte et al., 1989; Ahmed and Semmens, 1992b;
101 Matsuda et al., 1999; Ahmed et al., 2004). However, few studies have tried to

102 concurrently improve the OTR and OTE. A novel approach may be periodically
103 opening the membranes to vent back-diffusion gases. This will allow the back-diffusion
104 gases to be vented to the atmosphere during the open phase, re-establishing the uniform
105 almost constant gas pressure profile along the fiber length.

106 Previous research experimentally explored increasing the gas flow rates, or intermittent
107 degassing processes (Li et al., 2010; Castagna et al., 2015). Fang et al., (2004) measured
108 and modeled the gas composition inside a membrane, and gave modeled predictions of
109 gas concentration profiles as a function of time applying when supplied with a pulsing
110 strategy. However, they did not systematically explore the impacts of the pulsing
111 frequency on the OTE and OTR, and their model was only applicable under conditions
112 of liquid creeping flow.

113 The objective of this study was to use experiments and modeling to systematically
114 explore periodic venting of hollow-fiber membranes as a means to maximize the OTE
115 and OTR of MABRs.

116

117 **2. MATERIALS AND METHODS**

118

119 Our strategy was to (1) experimentally study OTRs and OTEs for “clean” HFMs (i.e.,
120 without biofilm), for open end, closed end, and for periodic venting, (2) use
121 mathematical modeling to expand the experimental findings and predict the effects of
122 periodic venting for a clean HFM, and (3) experimentally assess the periodic venting
123 strategy for an MABR (i.e., a HFM with biofilm). OTR was calculated as the oxygen
124 flux difference between the inlet and the outlet which corresponds to the flux of oxygen
125 transferred across the membrane surface. OTE was calculated as the flux difference

126 divided by the inlet flux. OTE represents the percentage of the transferred oxygen flux
127 with respect to the supplied oxygen. Fluxes were estimated according to equation (1).

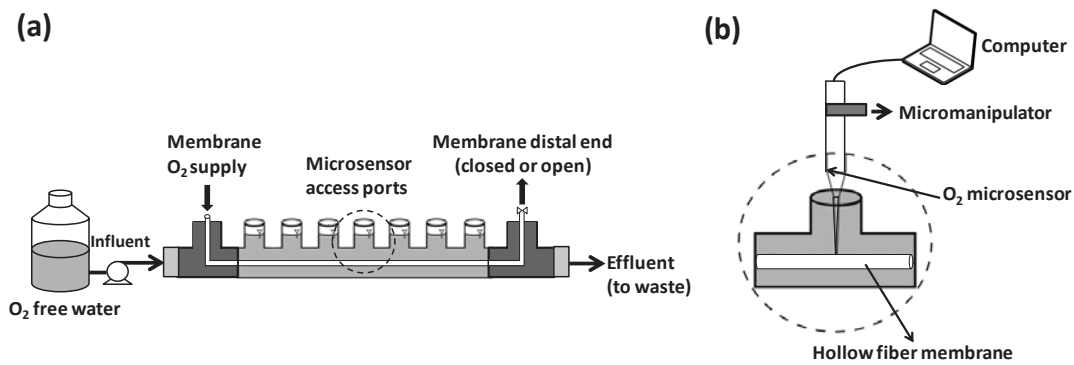
128

129 **2.1 Experimental flow cells configuration**

130 An experimental flow cell with a single HFM was used to explore OTRs and gas back
131 diffusion in clean HFMs, i.e., without biofilm. The flow cell consisted of square-section
132 glass tube with 6-mm inside dimension, and 40-cm length. The flow cell had seven
133 ports for dissolved oxygen (DO) measurements (Figure 2), separated 3.8 cm along the
134 flow cell. Water was deoxygenated by nitrogen sparging and pumped through the flow
135 cell using a peristaltic pump (Cole Palmer, Vernon Hills, IL, USA).

136 Tests were first carried out to determine the HFM's mass transfer coefficient. To test
137 the mathematical model, experiments were then performed with a range of water
138 velocities, oxygen supply pressures, feed gases (air and pure oxygen), water flow
139 directions (co-current or counter current with respect to the inlet gas supply), and
140 transient shifts between open and closed ends.

141 The flow cell used a composite, microporous polyethylene membrane with a dense 1
142 μm polyurethane core (HFM200TL, Mitsubishi Rayon, Japan). The outer diameter was
143 280- μm and the wall thickness was 40- μm . A single membrane was located in the
144 middle of the flow cell, supported at both ends by a gas-supplying manifold. The gas
145 was supplied from one end at constant pressure, while a valve at the opposite end
146 allowed open or closed operation of the membrane. Pure oxygen or air was supplied at
147 0.07 or 0.18 atm relative pressure. The influent flow rate ranged from 2 to 10 mL/min,
148 resulting in a liquid velocity of 1 to 5 mm/s and a Reynolds number of 5 to 28, well
149 within the laminar flow regime.



150

151 **Figure 2.** (a) Schematic of flow cell. Oxygen-free water from a reservoir was pumped into the square-
 152 section glass tube with a hollow-fiber membrane supplied with O₂ or air in the middle. (b) Detail of a
 153 flow-cell port used for DO measurement with a microsensor controlled by a micromanipulator.

154

155 Two separate reactors were used for the MABR tests, with the same configuration as
 156 described above. Reactor MABR-1 was operated with an open-ended membrane, while
 157 MABR-2 was initially operated with a closed end, but later was operated with periodic
 158 opening to vent lumen gases. De-oxygenated synthetic media (described below) was
 159 pumped through the flow cell. Each MABR had a recirculation pump and was
 160 connected to a purging reservoir, where the bulk liquid was sparged with N₂ to strip any
 161 residual DO from the reactor. Bulk liquid N₂ bubbles were vented in the reservoir
 162 before recycle line back to the flow-cell. This avoided any DO accumulation in the bulk
 163 liquid, which was a concern in the initial stages, prior to biofilm development. A
 164 magnetic stir bar kept the reservoir well-mixed with a high shear velocity, minimizing
 165 the attachment of biomass to the glass surface. An influent flow rate of 1 mL/min and a
 166 recirculation of 60 mL/min were provided to each MABR. Pure oxygen was supplied to
 167 the lumen of each at 0.05 atm relative pressure.

168

169

170 **2.2 Synthetic medium for the MABRs**

171 The synthetic wastewater for MABR-1 and MABR-2, was prepared from distilled water
172 amended with 2.773 g Na_2HPO_4 , 0.169 g KH_2PO_4 , 0.410 g $\text{MgSO}_4 \cdot 7\text{H}_2\text{O}$ and 0.202
173 g $(\text{NH}_4)_2\text{SO}_4$ per liter, as well as a trace mineral and calcium iron solutions. Ca-Fe
174 solution contained, per liter: 1 g $\text{CaCl}_2 \cdot 2\text{H}_2\text{O}$ and 1 g $\text{FeSO}_4 \cdot 7\text{H}_2\text{O}$. The trace mineral
175 solution contained, per liter: 100 mg $\text{ZnSO}_4 \cdot 7\text{H}_2\text{O}$, 30 mg $\text{MnCl}_2 \cdot \text{H}_2\text{O}$, 300 mg
176 H_3BO_3 , 200 mg $\text{CoCl}_2 \cdot 6\text{H}_2\text{O}$, 10mg $\text{CuCl}_2 \cdot 2\text{H}_2\text{O}$, 10 mg $\text{NiCl}_2 \cdot 6\text{H}_2\text{O}$, 30 mg
177 $\text{Na}_2\text{MoO}_4 \cdot 2\text{H}_2\text{O}$, and 30 mg Na_2SeO_3 . Potassium acetate was added as a COD source to
178 achieve 30 mgCOD/L. The synthetic wastewater was maintained anoxic by sparging the
179 medium with nitrogen gas and maintaining a positive pressure of nitrogen gas on the
180 storage container. The pH was maintained at approximately 7, while the water
181 temperature was 22 °C.

182 **2.3 Analytical methods**

183 Chemical oxygen demand (COD) was monitored in the influent and effluent of the
184 MABR reactors using colorimetric methods (Hach, Loveland, CO, USA). A glass
185 electrode pH meter was used to monitor pH.

186 For determining the biofilm thickness, we used a stereo-zoom light microscope (Cole-
187 Palmer, Chicago, IL) equipped with a mounted digital camera (Cybershot DSC-F707,
188 Sony) and a fiber-optic light source. The camera was fixed to the microscope with a 1×
189 mounting adapter. Biofilm thicknesses were measured using a microsensor by attaching
190 it to a motorized micromanipulator with a vertical resolution of 0.010 mm. The
191 microsensor tip was first positioned at membrane surface. Then, the tip was raised with
192 the computer-controlled motor until the tip reached the outer edge of the biofilm, which
193 was checked visually by microscopy. The distance was measured and recorded by

194 SensorTrace Suit software (Unisense). Biofilm image acquisition was also performed in
195 all seven flow-cell ports after four weeks of operation. Image processing for each
196 measurement was followed by statistical evaluation of the results.

197

198 **2.2 DO measurements**

199 Clark-type oxygen microsensors (Unisense A/S, Denmark) with a 10 μm tip diameter
200 were used to measure DO concentrations. The microelectrode movement was controlled
201 with a micro-manipulator (Model MM33-2, Unisense A/S). The use of microsensors is
202 an invasive method that can slightly affect the results. However, considering that the tip
203 was only 10 μm diameter and was immersed in a much thicker boundary layer, the
204 microsensors would be expected to have a minimal impact on the DO concentration.
205 Hydrodynamic measurements made by Hondzo et al., (2005), using a similar DO
206 microsensor diameters and Reynolds number as used in this study, concluded that the
207 disturbance of the flow by microsensors stem was minimal.

208 Longitudinal profiles of DO at the HFM surface were collected from the seven ports
209 once the system reached steady state, typically after two hours. For each port,
210 transversal DO profiles were collected starting from the HFM surface, across the liquid
211 diffusion layer (LDL), and into the bulk. The transversal DO measurements were
212 collected at 20- μm intervals, typically reached a distance of around 1000 μm from the
213 membrane surface. Profiles were collected at least in triplicate. For transient conditions,
214 DO was measured continuously at the membrane surface, for one of the intermediate
215 ports, during the shift from open-end to closed-end operation. Longitudinal steady-state
216 DO profiles were also taken in both MABRs after four weeks of operation.

217

218 **2.3 Calculation of membrane mass transfer coefficient, K_m**

219 The membrane mass transfer coefficient, K_m , was calculated from oxygen transfer tests
 220 in clean membranes. We used measured transversal DO profiles in the diffusion-
 221 dominated liquid boundary layer, using the flux continuity condition. The oxygen flux
 222 across the HFM, $J_{O_2,m}$, is equal to the diffusion flux through the mass transfer boundary
 223 layer at the membrane surface, $J_{O_2,l}$, as follows:

$$224 \quad J_{O_2,m} = K_m (C_{O_2,m(g)} - C_{O_2,m(l)}) = D_{O_2,l} \left. \frac{dC_{O_2,l}}{dr} \right|_{r=R_m} = J_{O_2,l} \quad (1)$$

225 where $D_{O_2,l}$ is the diffusion coefficient in the liquid phase (water), $C_{O_2,l}$ is the measured
 226 oxygen concentration in water, $C_{O_2,m}$ is the oxygen concentration in the microporous
 227 membrane on (g) gas side and (l) liquid side, and R_m the outer radius of the membrane.
 228 Given the small membrane thickness relative to the HFM radius, the membrane was
 229 approximated as a planar surface. From eq. (1) the oxygen mass transfer coefficient in
 230 the membrane is calculated as:

$$231 \quad K_m = \frac{D_{O_2,l} \left(\frac{dC_{O_2,l}}{dr} \right)_{r=R_m}}{C_{O_2,m(g)} - C_{O_2,m(l)}} \quad (2)$$

232 The oxygen diffusivity in water $D_{O_2,l}$ was obtained from the literature (Haynes et al.,
 233 2015). The oxygen concentration in the gas side of the microporous membrane, $C_{O_2,m(g)}$,
 234 is linked, by the ideal gas law, to the applied pressure and gas composition y_{O_2} (either
 235 O_2 or air, at the working temperature). When determining the K_m , the HFM was
 236 operated in open end mode to minimize concentration changes. Also, microsensor
 237 measurements were carried out at the first port of the flow cell (from the left side),
 238 where the gas concentration was essentially equal to the supply concentration,
 239 $C_{O_2,m(g)} = p y_{O_2,in} / (RT)$. The oxygen gas concentration in the membrane, where it
 240 contacts the liquid, is related to the DO concentration in the liquid by the partition

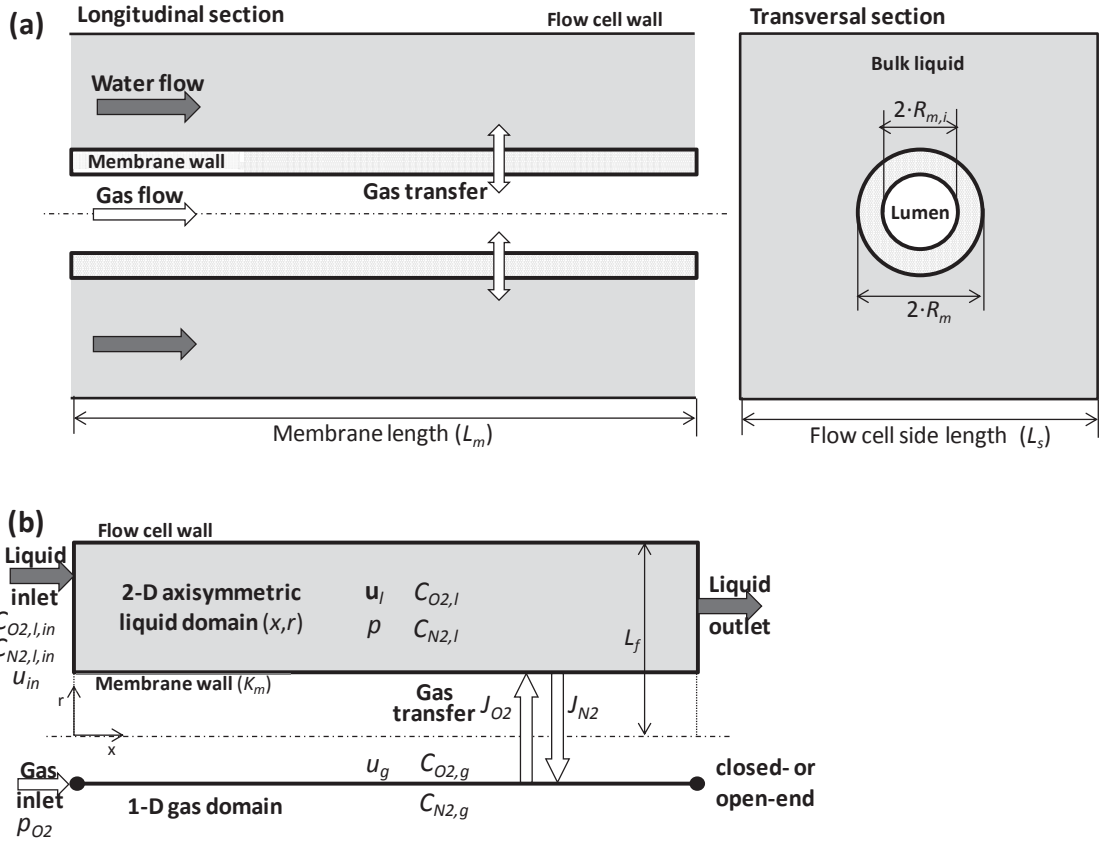
241 equilibrium (Henry's law), such that $C_{O_2,m(l)} = (C_{O_2,l})_{r=R_m} / H_{O_2}$. Finally, microsensor
242 measurements of concentration profiles of DO in water were used to determine the
243 concentration gradient at the membrane surface, $(dC_{O_2,l} / dr)_{r=R_m}$ and the concentration
244 $(C_{O_2,l})_{r=R_m}$. As mentioned above, profiles were collected at least in triplicate, and the
245 reported K_m is the average of the replicates.

246

247 **2.4 Numerical model for gas back-diffusion**

248 A mathematical model for gas back-diffusion was developed, addressing both steady-
249 state and transient conditions. The model included O₂ supply from the HFM lumen, and
250 assumed that the bulk liquid was in equilibrium with 1 atm of N₂. The model was
251 implemented with the finite-element simulation platform COMSOL Multiphysics
252 (COMSOL 4.4, Comsol Inc., Burlington, MA, www.comsol.com).

253 The numerical model included fluid flow and mass transport of O₂ and N₂, both in the
254 liquid surrounding the HFM and in the lumen gas (Figure 3). For the flow and mass
255 transport in the liquid phase, a two-dimensional (2-D) axisymmetric geometry was set
256 along the axis of the membrane lumen (direction x) with radial gradients along direction
257 r. The 2-D model implies an annular cross-section for the flow, with size $L_f = 3.4$ mm
258 (the radius of a circle with the same area as the square cross-section). This model was
259 coupled with a one-dimensional (1-D) domain for gas flow and mass transport in the
260 membrane lumen (assuming no radial gradients in the lumen).



261

262 **Figure 3.** (a) Schematic representation (not at scale) of the experimental co-current aeration system with
 263 a single HFM inside a square-section flow cell filled with liquid. Water flows between the HFM and the
 264 flow cell wall, and the membrane is supplied with oxygen. (b) Model representation including a 2-D
 265 axisymmetric liquid domain connected via the membrane wall with a 1-D gas domain.

266

267 2.4.1 Flow and mass transport in the liquid

268 The liquid velocity distribution in the flow cell was determined by solution of the two-
 269 dimensional Navier-Stokes equations (3) and (4) in the 2-D axisymmetric domain:

$$270 \quad \rho(\mathbf{u}_l \cdot \nabla) \mathbf{u}_l = \nabla \cdot \left[-p \mathbf{I} + \mu (\nabla \mathbf{u}_l + (\nabla \mathbf{u}_l)^T) \right], \quad \nabla \cdot \mathbf{u}_l = 0 \quad (3),(4)$$

271 where \mathbf{u}_l is the water flow velocity, p is the pressure, ρ is the water density, μ is the
 272 liquid dynamic viscosity, and \mathbf{I} is the identity matrix. The water velocity was assumed to
 273 be zero at the membrane surface and at the flow cell wall (non-slip condition, $\mathbf{u}_l=0$).

274 Laminar flow conditions were imposed, with average velocity u_{in} in the inlet and zero
 275 relative pressure in the outlet.

276 The mass transport of oxygen and nitrogen in the liquid flow results from convection-
 277 diffusion equations (5) and (6) solved for the dissolved O₂ and N₂ concentrations, $C_{O_2,l}$
 278 and $C_{N_2,l}$:

$$279 \quad \mathbf{u}_l \nabla C_{O_2,l} = D_{O_2,l} \nabla^2 C_{O_2,l}, \quad \mathbf{u}_l \nabla C_{N_2,l} = D_{N_2,l} \nabla^2 C_{N_2,l} \quad (5),(6)$$

280 where $D_{O_2,l}$ and $D_{N_2,l}$ are the diffusion coefficients in the liquid. Constant dissolved O₂
 281 and N₂ concentrations were imposed at the inlet boundary, $C_{O_2,l,in}$ and $C_{N_2,l,in}$. N₂ was
 282 present in the feed water at 18 mg/L, which corresponds to equilibrium with 1 atm of
 283 N₂. Convection-only outlet boundary was assigned ($\partial C_{O_2,l} / \partial x = \partial C_{N_2,l} / \partial x = 0$), while
 284 no-flux conditions were imposed at the flow cell wall ($\partial C_{O_2,l} / \partial y = \partial C_{N_2,l} / \partial y = 0$). On
 285 the membrane wall, flux continuity conditions were set:

$$286 \quad J_{O_2} = K_m (C_{O_2,g} H_{O_2} - C_{O_2,l}), \quad J_{N_2} = K_m (C_{N_2,g} H_{N_2} - C_{N_2,l})$$

287 where H_{O_2} and H_{N_2} are the gas-liquid partition (Henry's) coefficients at 20 °C. We
 288 assumed that the membrane, which was microporous, had the same selectivity for O₂
 289 and N₂ (Ahmed and Semmens, 1992a), which translates to the same K_m .

290

291 2.4.2 Flow and mass transport in the gas

292 The mass balances for the gases in the membrane lumen were adapted from Ahmed and
 293 Semmens (1992a), who modeled steady-state O₂ and N₂ profiles in a closed-end HFM.
 294 Unlike the past model, our model includes transient behavior, and used computational
 295 fluid dynamics to determine dissolved gas concentrations in the fluid along the

296 membrane length. Frictional gas pressure losses in the lumen were included, and the
 297 model allowed for transient conditions to be simulated, for example when switching
 298 from open-end to closed-end operation. Finally, the membrane mass transfer resistance
 299 (K_m) was considered explicitly. Note that only longitudinal gradients in gas
 300 concentrations (direction x) were considered in our model.

301 In both closed-end and open-end operation, the one-dimensional transient mass balances
 302 for O_2 (eq.(7)) and N_2 gas (eq.(8)) in the membrane lumen included transport by
 303 convection and diffusion, and transfer across the wall into or from the liquid phase.
 304 These equations allowed the concentrations $C_{O_2,g}(t, x)$ and $C_{N_2,g}(t, x)$ to be calculated.

$$305 \quad \frac{\partial C_{O_2,g}}{\partial t} = \frac{\partial}{\partial x} \left(D_g \frac{\partial C_{O_2,g}}{\partial x} - u_g C_{O_2,g} \right) - \frac{2}{R_m} K_m (C_{O_2,g} H_{O_2} - C_{O_2,l}) \quad (7)$$

$$306 \quad \frac{\partial C_{N_2,g}}{\partial t} = \frac{\partial}{\partial x} \left(D_g \frac{\partial C_{N_2,g}}{\partial x} - u_g C_{N_2,g} \right) - \frac{2}{R_m} K_m (C_{N_2,g} H_{N_2} - C_{N_2,l}) \quad (8)$$

307 In eq. (7) and (8), u_g is the gas velocity in the fiber, while $C_{O_2,l}$ and $C_{N_2,l}$ are the
 308 corresponding dissolved O_2 and N_2 concentrations, respectively, at position x . The same
 309 mass transfer coefficient through the membrane, K_m , and the same diffusion coefficient
 310 in the gas phase, D_g , was assumed for both gases.

311 The gas velocity in the lumen was calculated differently for close-end or open-end
 312 operation. In the closed-end operation, frictional losses were neglected due to the very
 313 low gas velocity in the lumen. For this case, the sum of gas concentrations at any point x
 314 is equal to that of the inlet: $C_{O_2,g} + C_{N_2,g} = C_{O_2,in} + C_{N_2,in} = \text{constant}$. In these conditions,
 315 the sum of eq. (7) and (8) is equal to zero. Adding eq. (7) and (8), and rearranging,
 316 results in:

$$317 \quad \frac{du_g}{dx} = - \frac{2K_m (C_{O2,g} H_{O2} - C_{O2,l} + C_{N2,g} H_{N2} - C_{N2,l})}{R_m (C_{O2,in} + C_{N2,in})} \quad (9)$$

318 which allows for calculation of the local gas velocity along the fiber, $u_g(x)$, resulting
 319 from the diffusion of gasses into or out of the membrane. At the sealed end, the gas
 320 velocity must be zero ($u_g=0$ at $x=L_m$). The inlet concentrations were calculated from the
 321 universal gas law, for example, $C_{O2,g,in} = p y_{O2,in} / (RT)$ with $y_{O2,in}$ the oxygen fraction in
 322 the inlet gas (i.e., 1 for pure oxygen or 0.21 for air). In model simulations for the
 323 parametric study, only pure oxygen was used, i.e., $C_{N2,g,in}=0$.

324 For the open-end HFM, the constant gas velocity u_g was calculated from the Hagen-
 325 Poiseuille relationship, which is valid for slightly compressible fluids (Federspiel et al.,
 326 1996):

$$327 \quad u_g = \frac{R_{m,i}^2}{8\mu_g L_m} (p_{in} - p_{out})$$

328 where μ_g is the gas dynamic viscosity and $R_{m,i}$ is the internal fiber radius. The inlet
 329 pressure p_{in} was defined according to the measured value, while the outlet pressure p_{out}
 330 was set as atmospheric pressure.

331 The boundary conditions for equations (7) and (8) imply constant concentrations in the
 332 inlet $C_{O2,g,in}$ and $C_{N2,g,in}$ at $x=0$. At $x=L_m$, zero diffusion was assumed for the open-end
 333 case, while for the closed-end zero total flux was imposed, which in both cases leads to:

$$334 \quad \frac{\partial C_{O2,g}}{\partial x}(t, x = L_m) = 0, \quad \frac{\partial C_{N2,g}}{\partial x}(t, x = L_m) = 0$$

335 Initial gas concentrations for the entire membrane were equal to the inlet concentrations.
 336 Predicted DO concentrations at the surface of the fiber ($C_{O2,l}$) were directly compared
 337 with experimental measurements for both steady and transient states. Several model

338 parameters were taken from the experimental conditions, such as membrane thickness,
 339 average water velocity, membrane length and radius, dissolved nitrogen, dissolved
 340 oxygen in the influent water, and oxygen gas pressures in the membrane inlet and
 341 outlet. For the model application, parametric studies were used, where simulations were
 342 carried out for a range of values of a single parameter. These and other parameters
 343 obtained from literature are summarized in Table 1.

344 **Table 1.** Model parameters

Parameter	Symbol	Value	Units	Reference
<i>Physical parameters</i>				
Water density	ρ	1000	kg/m ³	(Haynes et al., 2015)
Water dynamic viscosity	μ	0.001	Pa·s	(Haynes et al., 2015)
Gas dynamic viscosity	μ_g	$1.8 \cdot 10^{-5}$	Pa·s	(Haynes et al., 2015)
O ₂ diffusion coefficient in water	$D_{O_2,l}$	$2 \cdot 10^{-9}$	m ² /s	(Haynes et al., 2015)
N ₂ diffusion coefficient in water	$D_{N_2,l}$	$1.7 \cdot 10^{-9}$	m ² /s	(Haynes et al., 2015)
O ₂ and N ₂ diffusivity in gas	D_g	$1.76 \cdot 10^{-5}$	m ² /s	(Haynes et al., 2015)
Henry coefficient for O ₂	H_{O_2}	0.0338	mol(aq.)/mol(g)	(Haynes et al., 2015)
Henry coefficient for N ₂	H_{N_2}	0.0156	mol(aq.)/mol(g)	(Haynes et al., 2015)
Ideal gas constant	R	$8.206 \cdot 10^{-5}$	m ³ ·atm/(mol·K)	-
<i>Membrane parameters</i>				
Mass transfer coefficient	K_m	$5.4 \cdot 10^{-5}$	m/s	Fitted to experiments
Length	L_m	0.32 2.5	m m	Experimental Parametric study
Outer radius	R_m	140	μm	Mitsubishi Rayon
Inner radius	$R_{m,i}$	130	μm	Mitsubishi Rayon
<i>Operation conditions</i>				
Oxygen inlet liquid concentration	$C_{O_2,l,in}$	0	mol/m ³	Experimental

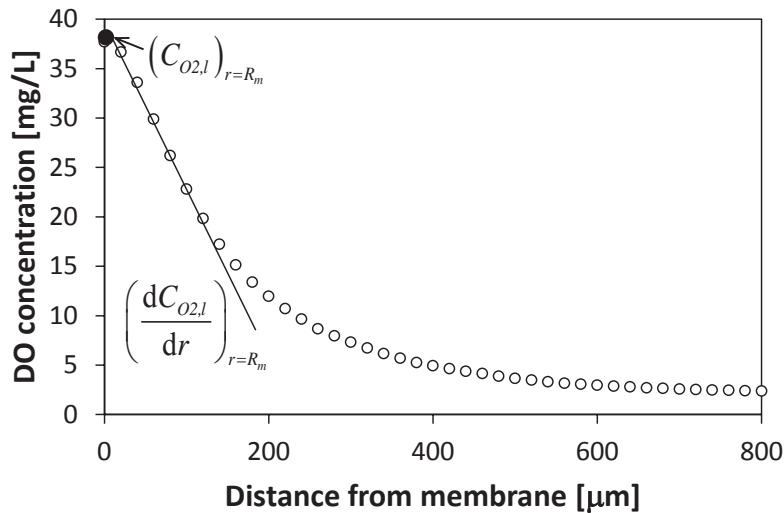
Nitrogen inlet liquid concentration	$C_{N_2,l,in}$	0.64	mol/m ³	Experimental
Oxygen inlet gas concentration	$C_{O_2,g,in}$	69.7	mol/m ³	Experimental
Nitrogen inlet gaseous concentration	$C_{N_2,g,in}$	0	mol/m ³	Experimental
Inlet gas pressure	p_{in}	1.07 and 1.18 1.68	atm atm	Experimental Parametric study
Outlet gas pressure (for open-end)	p_{out}	1	atm	Experimental
Average liquid velocity	u_{in}	1 and 5	mm/s	Experimental
Venting interval	t_c	1, 2, 5, 10 and 30	min	Parametric study
Venting open-end duration	t_o	20	s	Parametric study
Temperature	T	293.15	K	Experimental

345

346 **3. RESULTS AND DISCUSSION**

347 **3.1 Determination of membrane mass transfer coefficient**

348 A typical plot of measured DO profiles, perpendicular to the membrane surface, is
 349 shown in Figure 4. From the slope of the measured DO concentration profile, the flux of
 350 oxygen was calculated with eq. (1). Subsequently, the mass transfer coefficient K_m was
 351 calculated from eq. (2). An average K_m value of 5.4×10^{-5} m/s was obtained. This value
 352 is consistent with previously determined oxygen mass transfer coefficients for the same
 353 membrane (Ahmed et al., 2004) who found $K_m = 5 \times 10^{-5}$ m/s. In this study, the mass
 354 transfer coefficients for N₂ and O₂ were assumed to be equal.



355

356 **Figure 4.** A representative profile of measured dissolved oxygen concentration through the mass transfer
 357 boundary layer in the liquid adjacent to the membrane. From this profile, the concentration and the
 358 normal gradient of concentration at the membrane surface ($d=0$ from membrane, which means $r=R_m$ in
 359 the numerical model) were extracted to calculate K_m .

360

361 3.2 Model evaluation

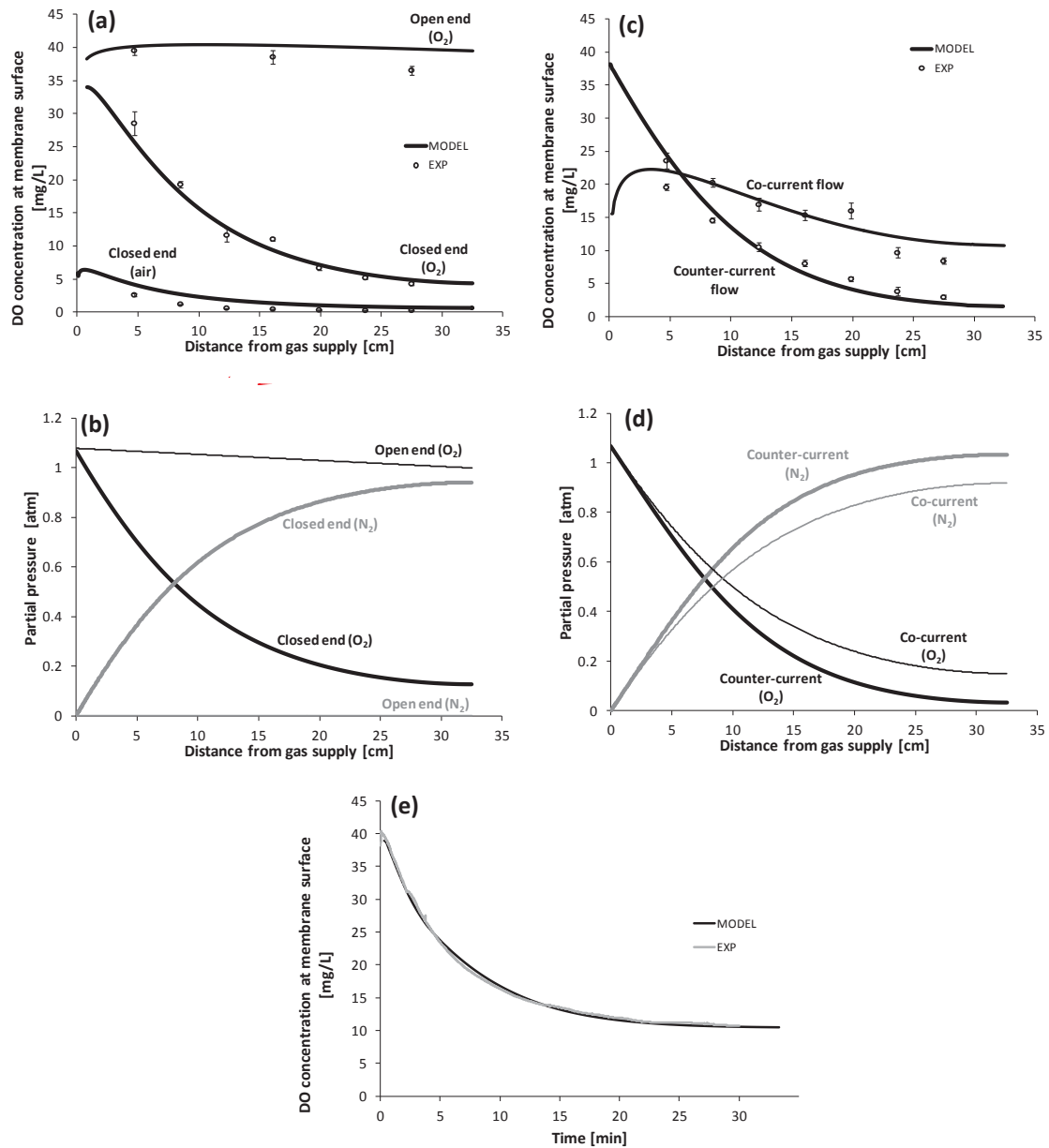
362 The back-diffusion model results were in good agreement with the measured values of
 363 DO along the membrane length, both for open- and closed-end operation, in steady state
 364 and transient conditions (Figure 5).

365 For closed ends using either air or pure O_2 supplied in co-current with the liquid flow
 366 ($u_{in} = 5$ mm/s), the N_2 back-diffusion significantly reduced the DO concentrations along
 367 the membrane length. The DO concentrations decreased from 35 mg/L to 5 mg/L when
 368 pure O_2 was supplied, and from 6 mg/L to 0.5 mg/L in case of air (Figure 5a).
 369 Accordingly, the steady state partial pressure of O_2 in the membrane lumen significantly
 370 decreased as O_2 was replaced by N_2 (Figure 5b). However, for the open-end operation,
 371 O_2 concentrations remained almost constant and at high values until the distal end of the
 372 membrane (Figure 5a). The open-end operation mode typically resulted in negligible

373 back-diffusion effects. The partial pressure of O₂ in the gas decreased only slightly
374 along the membrane because of the frictional pressure loss (Figure 5b).

375 The counter-current configuration showed lower DO concentrations towards the end of
376 the membrane than the co-current configuration, in stationary conditions at an average
377 water velocity of $u_{in} = 1$ mm/s (Figure 5c). When water flows in the opposite direction
378 of the supplied gas, i.e., in counter-current operation, O₂ transferred to the bulk liquid
379 from the membrane does not accumulate downstream of the flow cell, thus decreasing
380 DO concentrations in the liquid towards the closed end of the membrane. Therefore, the
381 rest of the simulations considered only co-current operation. The partial pressure of O₂
382 in the counter-current operation decreases more than in the co-current because of the
383 larger driving force for the trans-membrane transfer at the distal end, which is created
384 by the oxygen-free influent water.

385 The model also accurately predicted the transient behavior of the DO concentration after
386 suddenly closing the distal end of the membrane. The DO profile began with the steady
387 state value in open-end operation, and progressively decreased towards the steady state
388 value for the closed-end period. The experimental values and model predictions for the
389 Port 4 are shown in Figure 5e. The time required to reach a steady O₂ profile in the
390 lumen during the back-diffusion process was around 30 minutes.



391

392 **Figure 5.** Experimental and model-simulated dissolved oxygen (DO) profiles at the membrane surface for
 393 the experimental HFM flow cell. Liquid and gas flows are co-current, unless indicated otherwise. (a) DO
 394 profiles for open and closed end operation modes using an inlet relative gas pressure of 0.18 atm and
 395 $u_{in}=5$ mm/s. DO profiles for air and oxygen as supply gases are shown for the closed end cases; (b)
 396 Simulations of partial pressures for O_2 and N_2 in the open-end and closed-end with pure O_2 supply; (c)
 397 DO profiles along the membrane length for closed-end mode in co- and counter-current flow
 398 configurations using pure oxygen at 0.07 atm and $u_{in}=1$ mm/s; (d) Simulations of partial pressures for O_2
 399 and N_2 in the closed-end co- and counter-current operation with pure O_2 supply; (e) DO concentrations
 400 over time when transitioning from an open-end to a closed-end operation using pure O_2 at an inlet
 401 pressure of 0.18 atm. The microsensor measurement was performed at the membrane surface, for Port 4 at
 402 16.1 cm from the inlet. Error bars in plots (a) and (c) are the standard deviation of triplicate
 403 measurements.

404

405 **3.3 Model-based assessment of periodic venting**

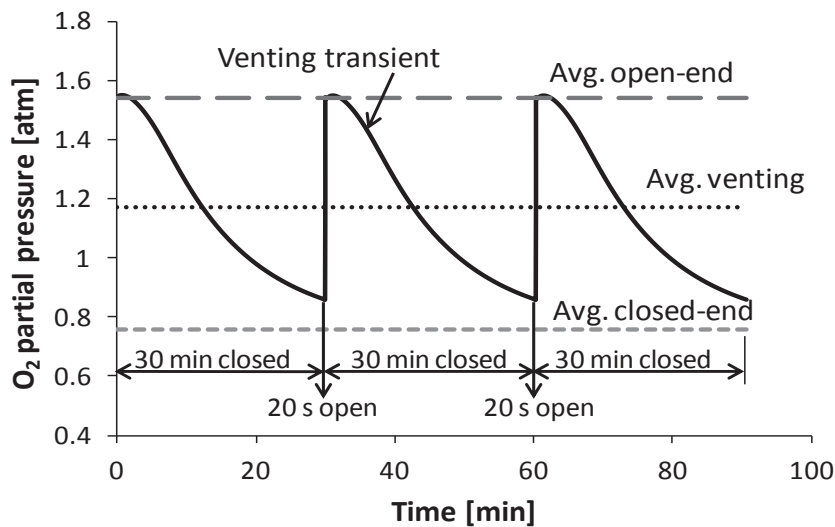
406 Closed-end HFMs initially have high gas transfer rates, as the membranes are filled
407 with pure O₂. However, the rates quickly decrease as gas back-diffusion profiles
408 develop. We used numerical modeling to study the effects of periodically venting
409 closed-end membranes, temporarily returning the membranes to the initial condition by
410 venting the back-diffusion gases. The transitory gas dynamics of periodic venting were
411 studied, and the impacts of different membrane opening intervals on OTRs and OTEs
412 were explored.

413 Time-averaged O₂ partial pressures during three venting cycles were calculated from
414 simulations with $R_m=140\ \mu\text{m}$, $K_m=5\times 10^{-5}\ \text{m/s}$, a longer membrane ($L_m=2.5\ \text{m}$) than in
415 the experimental setup (closer to what might be used in a full-scale MABR) and an inlet
416 gas pressure of $p_{in}=1.68\ \text{atm}$. Each cycle included a 30-minute closed period followed
417 by a 20-second open (venting) period. This corresponds to a 30-minute “venting
418 interval”. Figure 6 shows how, during the first cycle from $t=0$ to $t=30\ \text{min}$ (closed
419 phase), a drop in the membrane-averaged O₂ partial pressure developed due to back-
420 diffusion. Before the steady-state back-diffusion condition was fully obtained, the
421 membrane was opened for 20 seconds, allowing the O₂ partial pressures along the
422 membrane to recover their maximum value, which was slightly lower (1.54 atm) than
423 the inlet gas pressure due to the pressure drop resulting from high gas velocities in
424 open-end periods. The Hagen-Poiseuille relationship for slightly compressible fluids
425 effectively predicted the observed flows for a broad range of pressures, ranging from
426 0.07 to 0.68 atm (data not shown).

427 This periodic venting provides high OTEs during most of the cycle duration, while
428 maintaining higher time-averaged O₂ partial pressures than closed-end membranes.

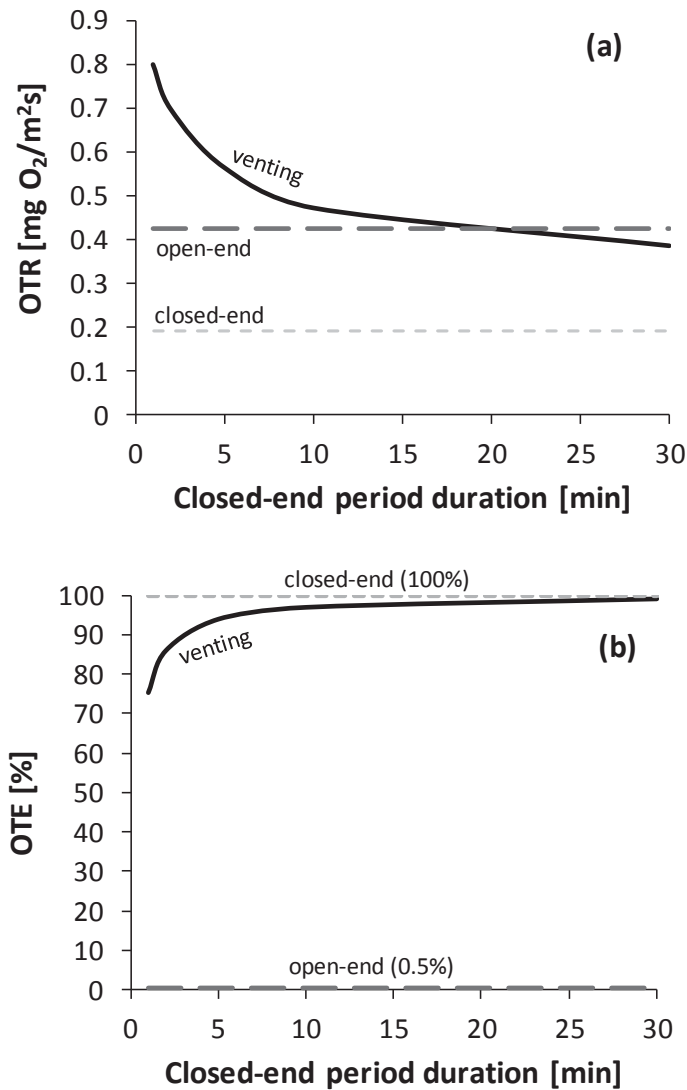
429 These results indicate that a 20-second open phase every 30 minutes was sufficient to
 430 allow oxygen pressure to recover its maximum value (1.54 atm) before the next closed
 431 phase. On the other hand, the membrane-averaged oxygen partial pressure dropped from
 432 1.54 to 0.86 atm during the closed-end phase. On average, the membrane had a higher
 433 O₂ pressure than in the steady-state, closed-end operation. Therefore, it provided a
 434 greater OTR than the purely closed-end mode.

435 To evaluate how the duration of the closed-end/open-end cycles influenced the OTRs
 436 and OTEs, we simulated different venting intervals (i.e., time between openings)
 437 ranging from 1 to 30 minutes, with a constant venting (open end) duration of 20 seconds
 438 (Figure 7). The predicted average OTRs were 2 to 4 times higher than with permanently
 439 closed end. Furthermore, the OTE values (75-99%) were comparable to the closed end
 440 (100%), and dramatically higher than the open end mode (0.5%).



441

442 **Figure 6.** Simulated O₂ partial pressures in the lumen, averaged along the entire membrane length for
 443 different operation regimes: (i) transient (solid line) and time-averaged (dotted line) during three venting
 444 cycles, (ii) steady state closed end (short-dashed gray line), and (iii) steady state open end (long-dashed
 445 gray line).



446

447 **Figure 7.** Comparison of simulated (a) oxygen transfer rates (OTR) and (b) oxygen transfer efficiencies
 448 (OTE) for open operation, closed operation, and intermittent opening. Venting mode was tested for
 449 venting intervals (time between ventings) ranging from 1 to 30 min, with 20 seconds open phases.

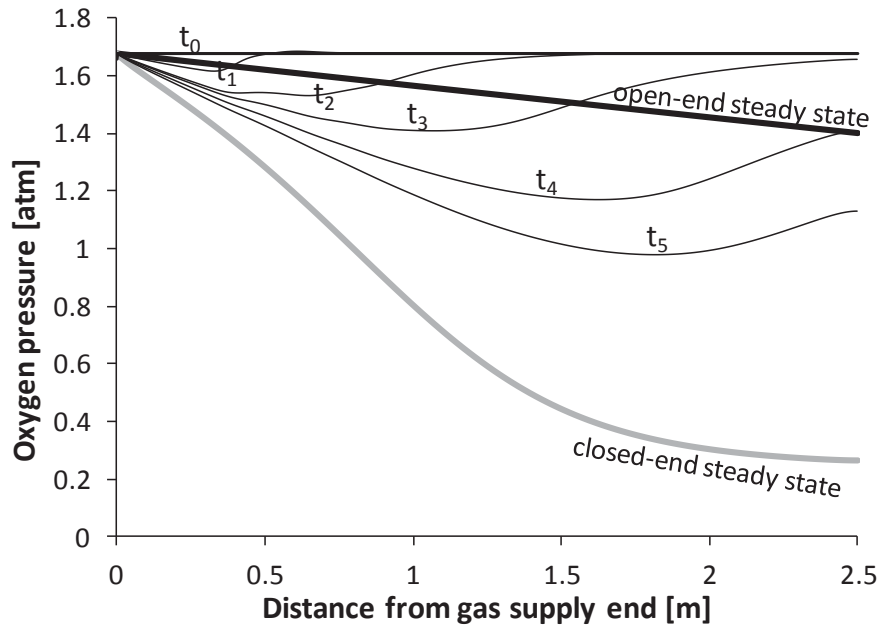
450

451 Interestingly, when the venting interval decreased below approximately 20 min, the
 452 OTR values were higher than for purely open-end operation, without significantly
 453 affecting the OTEs. This can be explained by the simulated O₂ pressure profiles along
 454 an HFM for open-end steady-state conditions, closed-end steady state conditions, and
 455 for the transition from open-end to closed-ended conditions (Fig 8). Profiles for the
 456 transition phase are presented at different times. For open-end operation, the O₂ pressure
 457 decrease is mainly due to frictional losses, whereas in closed-end operation the O₂

458 pressure drop is caused by back-diffusion. Furthermore, for the closed-end case, the O₂
459 concentration decreases from a constant initial value (equal to the inlet pressure of 1.68
460 atm), along the whole membrane until the steady state profile is reached. The shape of
461 the transient profiles shows that, initially, N₂ back-diffusion only affects the initial
462 portion of the HFM. This is where pure O₂ is supplied, and also where O₂-free water
463 enters the system, providing the maximum O₂ and N₂ concentration gradients. Then the
464 N₂/O₂ gas mixture is transferred by advective flow towards the distal end of the
465 membrane.

466 The time-dependent reduction in the O₂ pressure profiles occurs during the closed phase
467 of a venting cycle. If the venting interval is smaller, the time- and length-averaged O₂
468 pressure concentrations increase, leading to higher OTRs. However, below a certain
469 venting interval, the OTRs actually exceed those of the open-end configuration. This is
470 caused by the pressure drop resulting from high gas velocities in open-end
471 configuration. However, the pressure losses are negligible once the membrane is closed,
472 thus allowing a higher total average pressure inside the membrane (see pressure profiles
473 at times t_0 , t_1 , and t_2 in Figure 8).

474 The model results clearly indicate that periodic venting of closed-end operation can
475 improve the gas transfer rates beyond those obtainable with conventional open-end
476 operation, while maintaining high mass transfer efficiencies.



477

478 **Figure 8.** Oxygen partial pressure profiles along the membrane length for open-end (thick black line) and
 479 closed-end (thick gray line) steady state conditions, and time-averaged for transient conditions from open-
 480 to closed-end (thin black lines). The transient pressures are averages in time between the initial time and
 481 $t_1=2$ min, $t_2=5$ min, $t_3=10$ min, $t_4=20$ min, and $t_5=30$ min. Steady state conditions were essentially
 482 achieved after 60 minutes.

483 A simple calculation was made to compare different gas supply modes and show how
 484 the venting strategy could impact the MABR design, such as membrane area and
 485 required oxygen supply. Table 2 shows the OTRs, OTEs, required membrane areas, and
 486 O_2 supply needs using simulation results for the conditions in Figure 7. The membrane
 487 area was calculated for an arbitrary O_2 requirement. Oxygen supply requirements were
 488 determined by multiplying the OTE by the O_2 need. Finally, membrane areas and O_2
 489 supply requirements for open-end and venting modes were normalized to the values for
 490 closed-end operation (first row in Table 2). Calculations indicate that the open-end
 491 operation requires only half of the membrane area of the closed-end operation.
 492 However, around 200 times more O_2 is required. With the intermittent venting of 20
 493 seconds every 30 minutes, the required membrane area is the same as the open end, i.e.,
 494 half of the area required for the closed-end operation. But O_2 requirement is essentially
 495 the same as the closed-end operation.

496 **Table 2.** Required membrane areas and oxygen fluxes for closed-end, open-end, and venting modes.
 497 Areas and fluxes are normalized by the closed-end value.

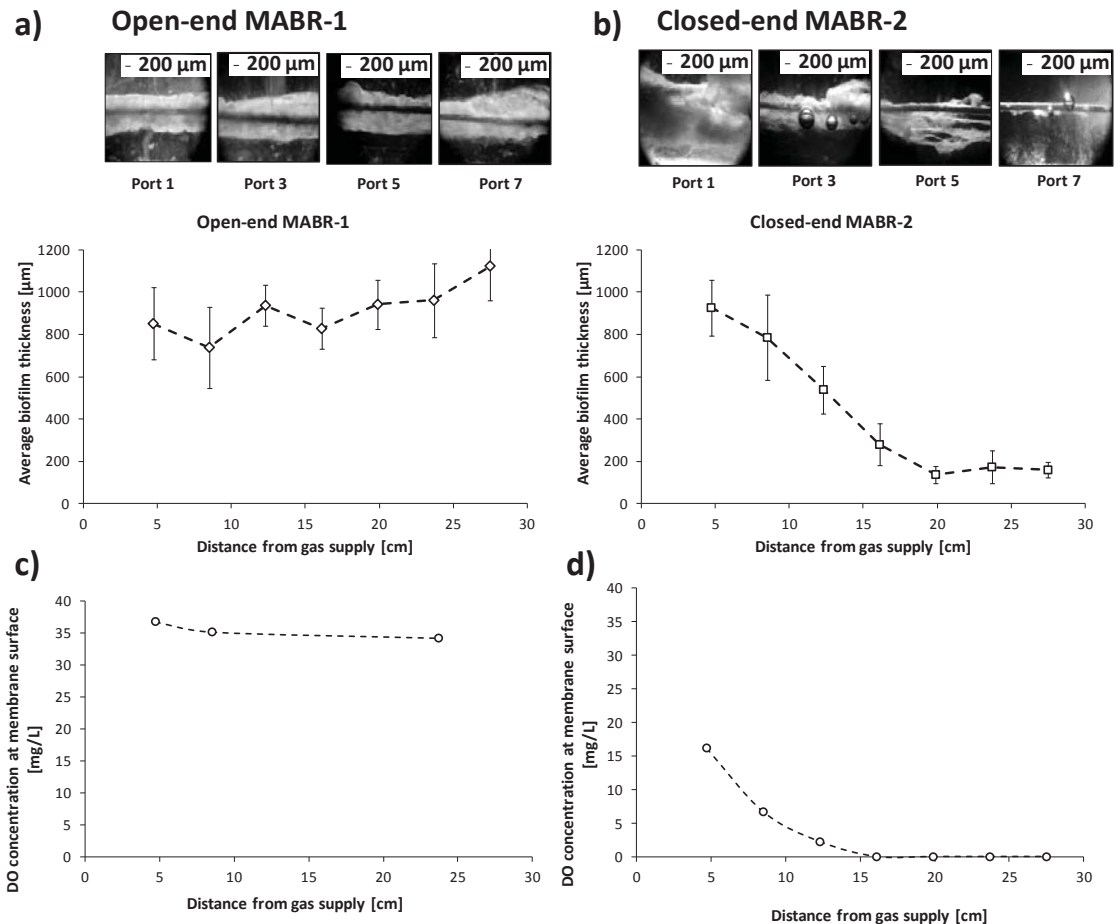
Case	OTR ($\text{mg m}^{-2}\text{s}^{-1}$)	OTE (%)	Normalized required membrane area	Normalized O ₂ supply requirement
Closed end	0.19	100	1.0	1.0
Open end	0.42	0.47	0.5	213
Venting ($t_c=1$ min, $t_o=20$ s)	0.79	75.3	0.2	1.3
Venting ($t_c=30$ min, $t_o=20$ s)	0.38	98.9	0.5	1.0

498

499

500 **3.4 Experimental assessment of gas supply strategies on HFMs with biofilm**

501 The periodic venting strategy was tested in a bench-scale MABR treating COD. Figure
 502 9 shows the biofilm thicknesses and measured DO concentration profiles along the
 503 membrane surface in two MABRs that were run in parallel. MABR-1 was operated in
 504 open-end mode, and MABR-2 was operated in closed-end mode. Biofilm thickness
 505 images and measurements of DO profiles were taken after four weeks of operation.

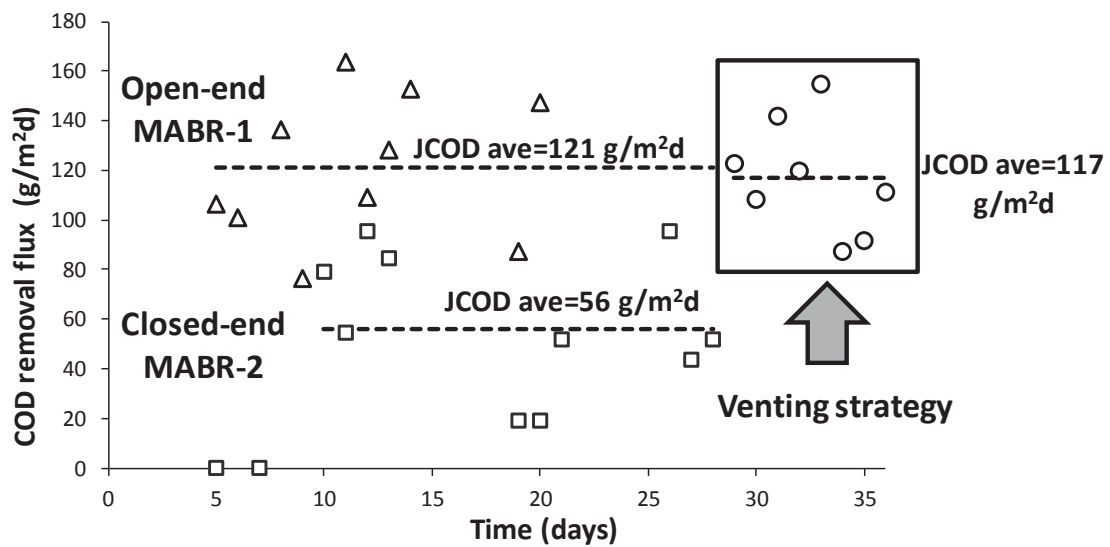


506

507 **Figure 9.** Biofilm thickness development along the membrane length in normally operated open-end
 508 MABR-1 (a) and closed-end MABR-2 (b). Experimental DO profiles at membrane surface for open-end
 509 MABR-1 (c) and closed-end MABR-2 (d). Port 1 is 4.7-cm from gas supply (left side), and Ports 3, 5, and
 510 7 are at 7.6-cm increments from Port 1.

511 In MABR-1 (open end), a homogeneous biofilm grew through the fiber surface, with a
 512 similar thickness along the membrane length (Figure 9a). In MABR-2 (closed end), the
 513 biofilm was thick at the gas supply end, but was significantly reduced towards the
 514 sealed end of the membrane (Figure 9 b). This can be explained by the measured DO
 515 profiles along the membrane (Figure 9 c and d). For MABR-1, the O₂ concentrations
 516 remained almost constant and at high values across the entire membrane (Figure 9 c).
 517 This is because the high supply gas rate into the membrane resulted in negligible back-
 518 diffusion effects. The partial pressure of O₂ in the gas decreased only slightly along the
 519 membrane because of frictional pressure loss. N₂ accumulation in the membrane was

520 not significant in MABR-1, as inlet gas flow-rate was high enough to vent back-
 521 diffused N_2 to the atmosphere. However, for MABR-2, O_2 consumption and N_2 back-
 522 diffusion significantly reduced O_2 concentrations along the fiber length (Figure 9 d)
 523 resulting in much lower OTRs and consequently lower overall COD removal fluxes
 524 (Figure 10).

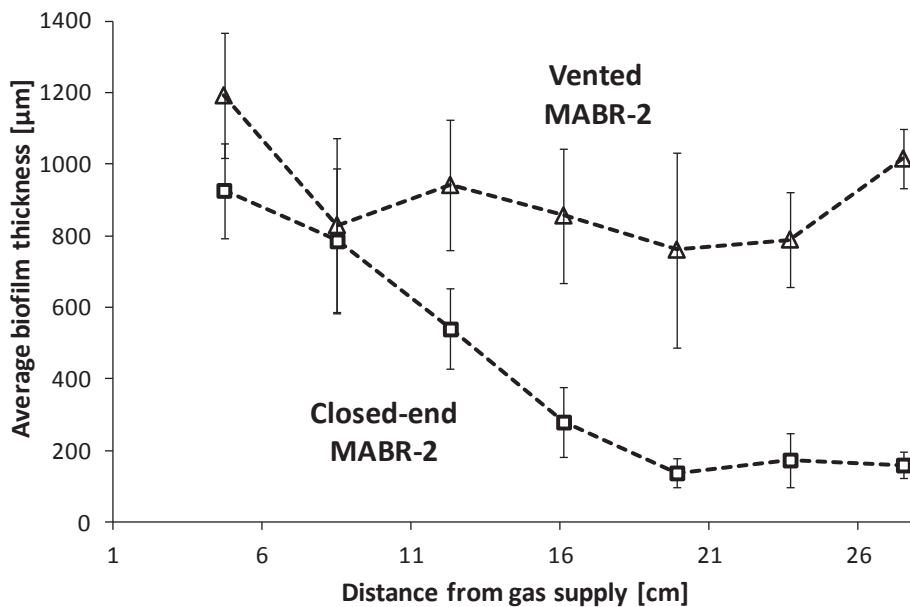


525

526 **Figure 10:** Experimentally observed COD removal fluxes in MABR-1 (triangles) and MABR-2 (squares)
 527 plotted against time. Circles enclosed in the black rectangle represent COD removal fluxes for the closed-
 528 end MABR-2 when a venting strategy of 20s open and 20 min closed was implemented.

529 The open-end MABR-1 had a higher average O_2 pressure than in the steady-state,
 530 closed-end MABR-2 (Figure 9 c and d). Therefore, it provided a greater OTRs and
 531 COD removal fluxes than the purely closed-end MABR-2 (Figure 10). The average
 532 COD removal flux for MABR-1 was double the value for MABR-2. In MABR-2, back-
 533 diffusion caused DO limitation in much of the membrane. This slowed the development
 534 of the biofilm, and consequently the increase in COD removal. Also, COD removal
 535 rates fluctuated considerably because this was a small reactor. As the biofilms grew, any
 536 biofilm detachment had a significant impact on the system. This would be more likely
 537 to average out in a larger system.

538 Note that the predicted OTR values for closed, open and venting strategies in a clean
 539 membrane were lower than those for MABRs. This is because the biofilm can eliminate
 540 the mass transfer resistance of the liquid concentration boundary layer (Semmens 2008).
 541 After four weeks of operation, MABR-2 was switched to periodic venting, which
 542 consisted of opening the membrane (venting) for 20 seconds every 20 minutes. Figure
 543 10 shows the experimental COD removal fluxes that were obtained when periodic
 544 venting cycles were applied to MABR-2. Figure 11 shows the biofilm thicknesses
 545 along the membrane length prior to venting, and after eight days of venting cycles.



546
 547 **Figure 11.** Biofilm thicknesses along the fiber length of MABR-2 just prior to initiating the venting
 548 cycles, and after eight days of periodic venting. Venting provides a much more uniform biofilm thickness.
 549 The mathematical model predicted that greater average O₂ partial pressures, and
 550 consequently higher OTRs and removal fluxes, could be obtained by applying periodic
 551 venting to a closed-end MABR. The experimental COD removal fluxes are shown in
 552 Figure 10. The average COD removal flux became double that for the closed-end
 553 operation, increasing from 56 gCOD/m²d to 117 gCOD/m²d. This value is very similar
 554 to the 121 gCOD/m²d obtained in MABR-1 (Figure 10). This was in part due to the

555 more uniform biofilm thickness along the length of the fiber when periodic venting was
556 implemented (Figure 11). Based on the measured gas flow rate through the membrane
557 during the open cycles, OTEs of at least 97% were obtained when applying the periodic
558 venting. In this research, the COD removal rates were greater than those obtained in
559 some previous MABR studies. This was mainly because we used pure oxygen as the
560 supplied gas. Also, we used acetate as organic carbon source. Acetate is readily
561 biodegradable substrate, as opposed to more complex organics such as wastewater.
562 Nevertheless, COD removal rates found in this study were similar than the ones
563 obtained by Osa et al. (1997), Pankhania et al. (1999) and Brindle et al. (1999), who
564 reported COD removal rate values in MABRs fed with pure O₂ of 180, 42.7, 62.6
565 gCOD/m²d respectively. Experimental results verified that periodic venting of closed-
566 end MABRs can lead to high OTRs and OTEs, improving the overall process
567 performance and increasing the energy efficiency.

568 This work highlights the potential transient behavior of gas back-diffusion, and the
569 potentially significant lag in reaching steady state operation after a perturbation. For
570 example, changing the supply gas pressure, concentration of supply gas in the liquid
571 phase, and concentration of back-diffusion gases in the liquid phase, among others.
572 Following any of these changes, it may take a considerable amount of time to reach
573 steady state.

574 The optimal venting interval (time between openings) and venting time (open period)
575 depends on a variety of factors, including the membrane mass transfer coefficient,
576 diameter, length, supply gas pressure and concentration, and dissolved gas
577 concentrations in the liquid. For instance, larger membrane diameters will likely allow a
578 greater venting interval, as there is greater gas storage in the membrane lumen relative

579 to the gas transfer across the membrane. Larger HFM diameters, and longer membrane
580 lengths, would require longer venting periods. When selective membranes are used, the
581 relationship between the diffusion coefficients can also be important. Finally, the effect
582 of liquid flow in a contactor, e.g., co-current, counter-current, or cross flow, can impact
583 the gas transfer rates and the transition to steady-state conditions. Future research
584 should explore the impact of the above factors in more detail.

585 Past research on MABRs has shown that water vapor can diffuse into the membrane and
586 condense at the sealed end, plugging part of the membrane (Côte et al., 1988; Côte et
587 al., 1989., Fang et al., 2004). However, it would take weeks or months for condensation
588 to have an appreciable effect on the membrane behavior. In our closed-end experiments,
589 the membranes were vented every two days, and no sign of condensate accumulation
590 was observed during the ventings. Some MABRs are periodically vented to remove
591 water condensation, but the frequency of venting is typically too low to obtain the gas
592 transfer rate benefits. Based on our findings, it would be easy to increase the venting
593 frequency to both remove condensate and obtain higher OTRs.

594

595 The above strategy was studied for O₂ supply to an MABR, but the periodic venting is
596 also relevant to MABRs supplied with air, or MBfR applications with gases such as
597 hydrogen gas (H₂) or methane (CH₄) (Martin and Nerenberg, 2012; Shi et al, 2013).

598 **4. CONCLUSIONS**

599 The periodic venting of lumen gases in a closed-end MABR can greatly improve the
600 membrane's OTRs and contaminant removal fluxes, without significantly impacting the
601 OTEs. This is due to the transient behavior of the lumen gas profiles when shifting

602 from open-end to closed-end operation. When the venting interval is short enough, the
603 OTR can be even higher than with continuous open-end operation. This novel gas
604 supply strategy can greatly increase the capacity of MABRs, and decrease the capital
605 and operating cost of new systems. Future research should address in more detail the
606 range of factors that affect the selection of opening interval, the closed duration, and the
607 impacts of these factors on the OTRs and OTEs.

608 **ACKNOWLEDGEMENTS**

609 Primary funding for this work was from Water Environment Research Foundation
610 (WERF) project U2R14. Additional funding was provided by the Basque Government,
611 partially financing Patricia Pérez, and the Spanish Ministry of Economics and
612 Competitiveness and the European Regional Development Fund (FEDER), project
613 “Innovative Integrated Biological Processes for Nutrients Removal (PBi2)” (CTM2012-
614 36227).

615

616 **REFERENCES**

- 617 Ahmed, T., Semmens, M.J., 1992a. The Use of Independently Sealed Microporous Hollow Fiber
618 Membranes for Oxygenation of Water - Model Development. *Journal of Membrane Science* 69(1-2), 11-
619 20.
- 620 Ahmed, T., Semmens, M.J., 1992b. Use of Sealed End Hollow Fibers for Bubbleless Membrane Aeration
621 - Experimental Studies. *Journal of Membrane Science* 69(1-2), 1-10.
- 622 Ahmed, T., Semmens, M.J., Voss, M.A., 2004. Oxygen transfer characteristics of hollow-fiber, composite
623 membranes. *Advances in Environmental Research* 8, 637-646.
- 624 Aybar, M., Pizarro, G., Boltz, J.P., Downing, L., Nerenberg, R., 2014. Energy-efficient wastewater
625 treatment via the air-based, hybrid membrane biofilm reactor (hybrid MfBR). *Water Science and*
626 *Technology* 69(8), 1735-1741.
- 627 Brindle, K., Stephenson, T., Semmens, M.J., 1998. Nitrification and oxygen utilisation in a membrane
628 aeration bioreactor. *Journal of Membrane Science* 144, 197-209.
- 629 Brindle, K., Stephenson, T., Semmens, M.J., 1999. Pilot-plant treatment of a high-strength brewery
630 wastewater using a membrane aeration bioreactor. *Water Environment Research*. 71 (6), 1197– 1204.
- 631 Castagna, L., Zanella, A., Scaravilli, V., Magni, F., Deab, S.A.E., Introna, M., Mojoli, F., Grasselli, G.,
632 Pesenti, A., Patroniti, N., 2015. Effects on membrane lung gas exchange of an intermittent high gas flow
633 recruitment maneuver: preliminary data in veno-venous ECMO patients. *Journal of Artificial Organs*
634 18(3), 213-219.

635 Côte, P., Bersillon, J.L., Huyard, A., 1989. Bubble-Free Aeration Using Membranes - Mass-Transfer
636 Analysis. *Journal of Membrane Science* 47(1-2), 91-106.

637 Côte, P., Bersillon, J.L., Huyard, A., Faup, G., 1988. Bubble-Free Aeration Using Membranes - Process
638 Analysis. *Journal Water Pollution Control Federation* 60(11), 1986-1992.

639 Downing, L.S., Nerenberg, R., 2008. Total nitrogen removal in a hybrid, membrane-aerated activated
640 sludge process. *Water Research* 42(14), 3697-3708.

641 Fang, Y., Clapp, L.W., Hozalski, R.M., Novak, P.J., Semmens, M.J., 2004. Membrane gas transfer under
642 conditions of creeping flow: modeling gas composition effects. *Water Research* 38(10), 2489-2498.

643 Federspiel, W.J., Henchir, K.A., 2004. *Encyclopedia of Biomaterials and Biomedical Engineering*,
644 Marcel Dekker, Inc., Pittsburgh, PA.

645 Federspiel, W.J., Williams, J.L., Hattler, B.G., 1996. Gas flow dynamics in hollow-fiber membranes.
646 *Aiche Journal* 42(7), 2094-2099.

647 Haynes, W.M., Bruno, T.J., Lide, D.R. (Ed.), 2015. *CRC handbook of chemistry and physics* CRC
648 Press/Taylor and Francis, Boca Raton, FL. Online at <http://www.hbcnetbase.com/>

649 Hibiya, K., Terada, A., Tsuneda, S., Hirata, A., 2003. Simultaneous nitrification and denitrification by
650 controlling vertical and horizontal microenvironment in a membrane-aerated biofilm reactor. *Journal of*
651 *Biotechnology* 100(1), 23-32.

652 Hondzo, M., Feyaerts, T., Donovan, R., and O'Connor, B.L. 2005. Universal scaling of dissolved oxygen
653 distribution at the sediment-water interface: A power law. *Limnology and Oceanography* 50, 1667-1676.

654 Jácome, A., Molina, J., Suárez, J., Tejero, I., 2006. Simultaneous Removal of Organic Matter and
655 Nitrogen Compounds in Autoaerated Biofilms. *Journal of Environmental Engineering* 132(10), 1255-
656 1263.

657 Martin, K.J., Nerenberg, R., 2012. The membrane biofilm reactor (MBfR) for water and wastewater
658 treatment: principles, applications, and recent developments. *Bioresource Technology* 122, 83-94.

659 Matsuda, N., Nakamura, M., Sakai, K., Kuwana, K., Tahara, K., 1999. Theoretical and experimental
660 evaluation for blood pressure drop and oxygen transfer rate in outside blood flow membrane oxygenator.
661 *Journal of Chemical Engineering of Japan* 32(6), 752-759.

662 Matsumoto, S., Terada, A., Aoi, Y., Tsuneda, S., Alpkvist, E., Picioreanu, C., van Loosdrecht, M.C.M.,
663 2007. Experimental and simulation analysis of community structure of nitrifying bacteria in a membrane-
664 aerated biofilm. *Water Science and Technology* 55(8-9), 283-290.

665 Nerenberg, R., 2016. The membrane-biofilm reactor (MBfR) as a counter-diffusional biofilm process.
666 *Current Opinion in Biotechnology* 38, 131-136.

667 Osa, J., Eguia, E., Vidart, T., Jácome, A., Lorda, I., Amieva, J., Tejero, I., 1997. Wastewater Treatment
668 with biofilm Membrane Reactors. In *Conference on Advanced Wastewater Treatment Processes*; Leeds
669 University; Leeds, UK, 1997.

670 Pankhania, M., Brindle, K., Stephenson, T., 1999. Membrane aeration bioreactors for wastewater
671 treatment: completely mixed and plug-flow operation. *Chemical Engineering Journal* 73(2), 131-136.

672 Roggy, D.K., Novak, P.J., Hozalski, R.M., Clapp, L.W., Semmens, M.J., 2002. Membrane gas transfer
673 for groundwater remediation: Chemical and biological fouling. *Environmental Engineering Science*
674 19(6), 563-574.

675 Satoh, H., Ono, H., Rulin, B., Kamo, J., Okabe, S., Fukushi, K., 2004. Macroscale and microscale
676 analyses of nitrification and denitrification in biofilms attached on membrane aerated biofilm reactors.
677 *Water Research* 38(6), 1633-1641.

678 Schaffer, R.B., Ludzack, F.J., Ettinger, M.B.C.F.p.d.S., 1960. Sewage Treatment by Oxygenation through
679 Permeable Plastic Films. *Journal (Water Pollution Control Federation)* 32(9), 939-941.

680 Semmens, M.J., 2008. Alternative MBR configurations: using membranes for gas transfer. *Desalination*
681 231(1), 236-242.

682 Semmens, M.J., Dahm, K., Shanahan, J., Christianson, A., 2003. COD and nitrogen removal by biofilms
683 growing on gas permeable membranes. *Water Research* 37(18), 4343-4350.

684 Shi Y, Hu S, Lou J, Lu P, Keller J, Yuan Z (2103). Nitrogen removal from wastewater by coupling
685 anammox and methane-dependent denitrification in a membrane biofilm reactor. *Environ Sci Technol*
686 2013, 47:11577-11583.

687 Syron, E., Casey, E., 2008. Membrane-aerated biofilms for high rate biotreatment: performance appraisal,
688 engineering principles, scale-up, and development requirements. *Environmental Science and Technology*
689 42(6), 1833-1844.

690 Tanishita, K., Nakano, K., Sakurai, Y., Hosokawa, T., Richardson, P.D., Galletti, P.M., 1978. Compact
691 Oxygenator Design with Curved Tubes Wound in Weaving Patterns. *Transactions American Society for*
692 *Artificial Internal Organs* 24, 327-331.

693 Terada, A., Hibiya, K., Nagai, J., Tsuneda, S., Hirata, A., 2003. Nitrogen removal characteristics and
694 biofilm analysis of a membrane-aerated biofilm reactor applicable to high-strength nitrogenous
695 wastewater treatment. *Journal of Bioscience and Bioengineering* 95(2), 170-178.
696 Timberlake, D.L., Strand, S.E., Williamson, K.J., 1988. Combined aerobic heterotrophic oxidation,
697 nitrification and denitrification in a permeable-support biofilm. *Water Research* 22(12), 1513-1517.
698 Weiss, P.T., Gulliver, J.S., Semmens, M.J., 1998. In-stream hollow-fiber membrane aeration. *Journal of*
699 *Hydraulic Engineering* 124(6), 579-588.
700 Weissman, M.H., Mockros, L.F., 1969. Oxygen and Carbon Dioxide Transfer in Membrane Oxygenators.
701 *Medical & Biological Engineering* 7(2), 169-184.
702
703

704